Journal of
Materials Chemistry A

PAPER

Cite this: *J. Mater. Chem. A*, 2025, **13**, 23893

Morphology tuned viologen-based covalent organic frameworks: a fast and targeted approach to eliminate toxic organic pollutants from water†

Pampa Jhariat,[b] Arjun Warrier,[b] Mebin Varghese[b] and Tamas Panda *[a]

Recent efforts to detoxify contaminated water with various materials have been met with limited success, largely due to an insufficient understanding of how material properties affect sorption performance. The application of porous materials with diverse morphologies in water decontamination has been ignored due to synthetic challenges and stability. Here, we report the synthesis of two chemically stable, crystalline viologen-based covalent organic frameworks (vBPDP and vMEL) with distinct morphologies; rod-shaped [vBPDP-8(R) and vMEL-7(R)] and spherical [vBPDP-7(S) and vMEL-8(S)], achieved by core plane modulations of the monomer (planar *vs.* nonplanar) and solvent polarity. We employed FESEM and HRTEM imaging of vBPDP at varying time intervals for a comprehensive analysis of the mechanisms of self-assembled morphologies. Furthermore, we compared the adsorption efficiencies of rod- and sphere-shaped vCOFs for removing anionic and neutral dyes from contaminated water. Rod-shaped vBPDP-8(R) and vMEL-7(R) demonstrated superior capture efficiencies compared to spherical vBPDP-7(S) and vMEL-8(S). vBPDP-8(R) achieved the highest capture of anionic dye methyl orange (1161.78 mg g^{-1}) and neutral dye fluorescein (1237.40 mg g^{-1}). DFT analysis confirmed strong non-covalent interactions between vCOFs and dyes, which strongly support our experimental results. Furthermore, the Quantum Theory of Atoms in Molecules (QTAIM) was employed to conduct a detailed atomic-level analysis of the interactions between vCOFs and dye molecules, providing insights into the nature of intermolecular contacts. This study uniquely explores the creation mechanisms and morphology-dependent performance of self-assembled vCOFs, emphasizing their potential in water treatment and material design.

Received 12th February 2025
Accepted 16th June 2025

DOI: 10.1039/d5ta01161b

rsc.li/materials-a

1. Introduction

The assertion that “Water is life” encapsulates this truth: life is impossible without water. Nevertheless, this resource that sustains existence is currently in jeopardy. Water pollution has significantly contributed to the grievous environmental damage caused by increased industrialization. One of the primary contributors to this water pollution is industrial effluent, which is abundant in organic/inorganic contaminants.[1] Many of these contaminants, including toxic organic dyes, are highly soluble in water, resistant to degradation, and pose toxic or carcinogenic risks for living beings.[2] To combat this, a wide range of materials, including carbons, zeolites, metal–organic frameworks (MOFs), coordination polymers, porous organic polymers (POPs) and covalent organic frameworks (COFs), have been explored as adsorbents for removing organic contaminants from water.[3–5] In this regard, ionic covalent organic frameworks are of great interest due to their charged, porous, rigid structures, which provide advantages over neutral frameworks. The rigid charge-based ionic framework allows the strong electrostatic force of attraction, which is ideal for host–guest interactions.[6,7] While significant efforts have been made to capture various toxic pollutants from wastewater using different porous materials, most of the studies primarily focus on the design and synthesis of novel materials. Therefore, their efficacies are frequently restricted by the lack of thorough understanding of the various physical properties (such as selectivity, kinetics and adsorption capacity) that generally influence the adsorption mechanisms.[8,9]

Exploring the potential of different physical properties to improve the efficacy of material sequestration is regarded as an effective approach in this context.

The surface morphology is one of the most critical factors that influence the physicochemical properties. Morphology modulation plays a pivotal role in nanoscience and nanotechnology, as it provides distinctive advantages that are not feasible through alternative modification methods, such as modifying

---

[a] Centre for Clean Environment, Vellore Institute of Technology, Vellore, Tamil Nadu-632014, India. E-mail: tamaskumarpanda@vit.ac.in

[b] Department of Chemistry, School of Advanced Sciences, Vellore Institute of Technology, Vellore, Tamil Nadu-623014, India

† Electronic supplementary information (ESI) available: Four supplementary videos. See DOI: **https://doi.org/10.1039/d5ta01161b**

molecular structures or building blocks. Minor adjustments to the morphological configurations can substantially influence surface area, adsorption behaviour, diffusion kinetics, and catalytic activity.[10–12] However, very limited attempts have been implemented in the area of covalent organic frameworks and polymers. Banerjee *et al.* showed the morphology variation tuned by supramolecular interactions within nanostructures that regulate the self-assembly process. Self-templation (template-free) and the formation of rigid and hollow structures are also key considerations in covalent organic assembly.[13] Self-templated synthesis is more cost-effective and considered superior to template-dependent methods. Consequently, a comprehensive understanding of the morphology-modulation in relation to its constituents is necessary, and molecular-level morphology engineering of ionic materials with identical chemical structures could be a promising strategy to adsorb contaminants from polluted water.[14–16] In this context, vCOFs are particularly advantageous due to their strong electrostatic interactions, easy synthesis, tunable functionalities, and high chemical stability.[17,18] Despite the suitability of vCOFs for such applications, the critical influence of finely tuned morphologies of these polymeric materials on toxic organic dye sequestration remains underexplored.

Under this backdrop, we have effectively synthesized two crystalline viologen-based covalent organic frameworks (vCOFs) that are chemically stable and exhibit distinct self-aggregated spherical and rod-shaped morphologies depending on the plane of the monomer core (planar or nonplanar) and the type of solvent used. Triazine-based vCOFs (vMEL) formed rigid spheres in mesitylene/water [vMEL-8(S)], while they were self-assembled into rods in the 1,4-dioxane/water [vMEL-7(R)] solvent mixture. In contrast, vCOFs based on triphenyl amines (vBPDP) exhibit the opposite behaviour, forming rod-shaped morphology in mesitylene/water [vBPDP-8(R)] and sphere-shaped morphology in the 1,4-dioxane/water [vBPDP-7(S)] solvent mixture (Fig. 1). The mechanisms of these self-assembled morphologies were thoroughly studied by FESEM and HRTEM imaging at various time intervals (12, 24, 36, 48, and 72 h). Different morphologies play a significant role in capturing organic dyes from contaminated water. Rod-shaped vBPDP-8(R) and vMEL-7(R) exhibited exceptionally high capture efficiencies towards anionic Methyl Orange (MO^-) and neutral Fluorescein (FL) dyes compared to spherical vBPDP-7(S) and vMEL-8(S). As per our knowledge, vBPDP-8(R) demonstrated the highest capture efficiency of 1237.40 mg g^{-1} and 1161.78 mg g^{-1} for FL and MO^- dyes, respectively, among the

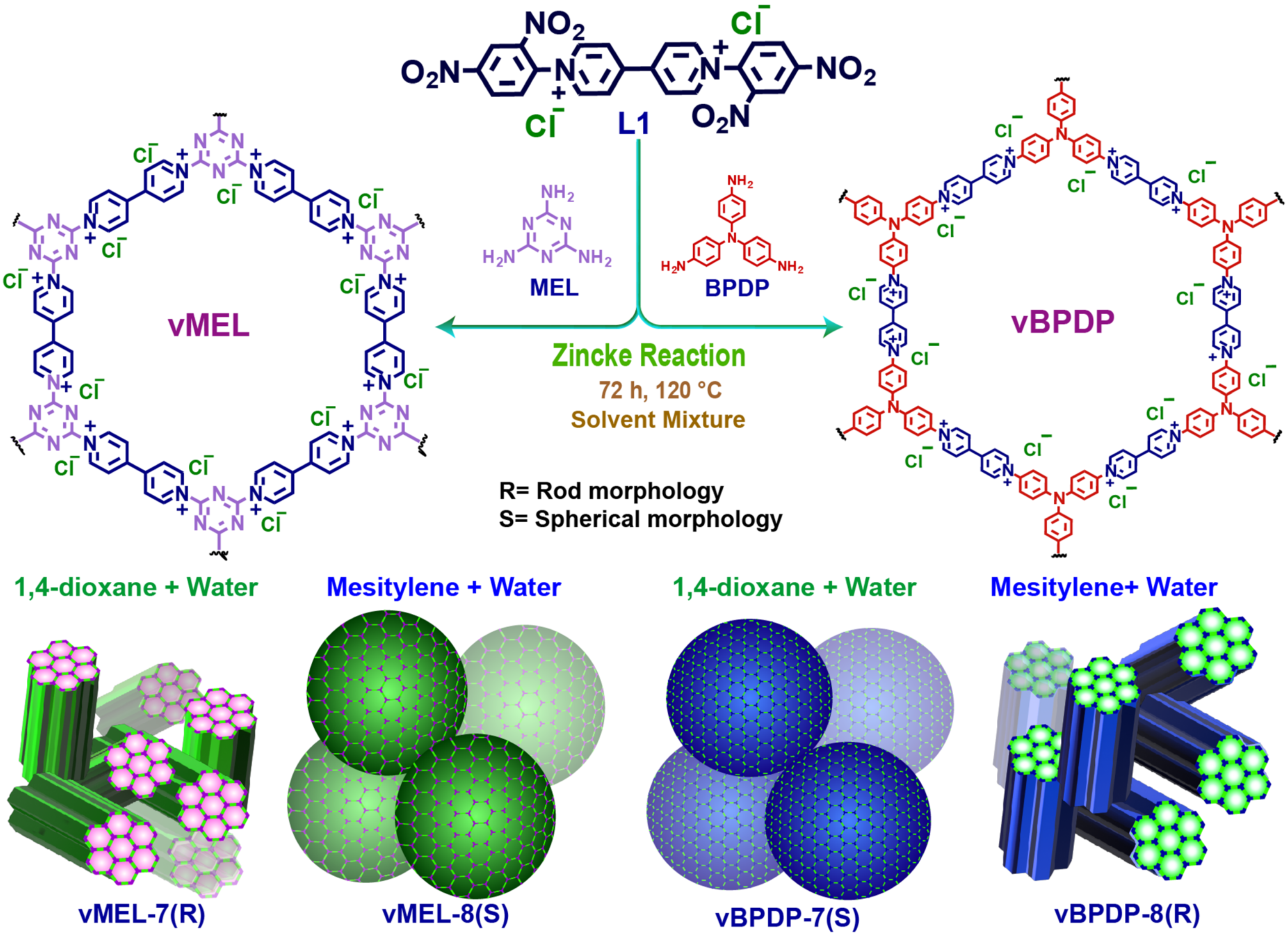

Fig. 1 Schematic representation of the synthesis of vMEL and vBPDP in two solvent mixtures (1,4-dioxane/water and mesitylene/water). We also represented schematically the diversity in morphology of vMEL and vBPDP (rod or spherical morphology) depending upon the solvent mixtures.

diverse sorbent materials reported so far. These results emphasize the influence of morphology on the adsorption efficiency of toxic dyes, which is also supported by DFT analyses that revealed robust non-covalent interactions with anionic and neutral dyes.

2. Results and discussion

2.1 Synthesis and characterization of vMEL and vBPDP

Synthesis of vMEL and vBPDP was carried out by the template-free solvothermal-assisted Zincke reaction at 120 °C for 72 h (detailed procedure in the Experimental section and Section II in the ESI†). In order to synthesize pure phase vMEL and vBPDP, a series of solvent mixtures were used for the solvothermal reaction (Table S1, ESI†). However, after several trials and errors, we found that the formation of pure crystalline products was successful when we used either dioxane + water (2 : 1) or mesitylene + water (4 : 1) as a solvent mixture. vMEL and vBPDP synthesized in the dioxane : water solvent mixture were named vMEL-7 and vBPDP-7. In contrast, vMEL and vBPDP synthesized in the mesitylene + water solvent mixture were named vMEL-8 and vBPDP-8, respectively. Furthermore, the products were collected and washed with several solvents (such as water, ethanol, DMAc, DMF, methanol and acetone) to obtain the pure-phase products. Additionally, the sample is incubated in a 1 : 1 mixture of $CHCl_3$ and THF for four days and subsequently degassed at 120 °C for 12 h. We used the degassed samples to carry out all the characterization studies. FT-IR spectra of all degassed vCOFs showed the absence of the peak at 1550 cm^{-1}, which corresponds to the NO_2 groups of the 2,4-dinitroaniline unit of linker L1 (Fig. S2†), corroborating the formation of the intended products through the Zincke reaction. Additionally, the absence of asymmetric and symmetric stretching bands at 3412 and 3437 cm^{-1}, associated with the amine group of the starting triamine precursor, further reinforced the completion of the polymerization process in the Zincke reaction. The solid-state ^{13}C CP-MAS NMR spectra of all vCOFs showed a broad signal between 110 and 170 ppm, indicating the presence of aromatic carbons in the polymeric networks of the structures. In vBPDP-7 and vBPDP-8, the carbons labeled as ‘a’ (Fig. S3†) displayed a more pronounced downfield chemical shift around 157 ppm, attributed to their conjugation with an aromatic ring and attachment to nitrogen. The pyridinium carbons exhibited chemical shifts in the regions marked as e, f, and g, ranging from 130 to 160 ppm. In contrast, in vMEL-7 and vMEL-8, the carbons labeled as ‘a’ (Fig. S4†) were shifted further downfield (approximately 170 ppm) due to the proximity of nitrogen atoms. It is crucial to note that crystalline viologen-based polymeric networks are extremely rare, with the majority of reports suggesting that such networks are amorphous in nature. Intriguingly, we found that vBPDP-7/-8 and vMEL-7/8 are crystalline in nature (Table S1, ESI†), as confirmed by experimental powder X-ray diffraction (PXRD) patterns. The experimental PXRD patterns of vBPDP-7 and -8 evidenced an assortment of crystalline peaks, which suggests an ordered framework alignment and long-range regularity (Fig. S5†). The presence of ordered 2D crystallites is confirmed by the peaks at $2\theta = 5.39°$, 9.97°, 12.68°, 16.36° and 23.44°, which are in good agreement with the previous report from our group.[19] In comparison with the simulated structures (Fig. S6†), the Pawley refinement of the experimental patterns for vBPDP-7 and vBPDP-8 demonstrated a satisfactory profile fit with $R_{wp} = 1.48\%$ and 1.36%, respectively. In contrast, the experimental PXRD patterns of vMEL-7 and vMEL-8 exhibit a crystalline peak at $2\theta = 2.36°$ and a small hump peak at 13.47° and 16.62°, including two low-intense peaks residing at 8.46°, and 9.67° (Fig. S7†). These results align well with the previously reported powder pattern of vMEL, confirming the presence of ordered 2D crystallites.[19] Compared to the simulated structures (Fig. S8†), the Pawley refinement of the experimental PXRD patterns for vMEL-7 and vMEL-8 showed a good profile match, with R_{wp} values of 3.54% and 1.24%, respectively. FESEM-EDX analysis and mapping (Fig. S9 and S10†) of all vCOFs clearly showcase the existing C, N and Cl ions homogeneously distributed among the structural moieties. In order to acquire a thorough comprehension of the chemical bonding characteristics of vCOFs, X-ray photoelectron spectroscopy (XPS) analysis was implemented. The XPS spectra of all four vCOFs demonstrated characteristic peaks that corresponded to C 1s, N 1s, and Cl 2p, thereby verifying the high purity of the samples (Fig. S11†). The N 1s spectra were deconvoluted into four components with binding energies of 398.5, 400.5, 402.5, and 406.0 eV (Fig. S11†). The 398.5 eV peak is indicative of tertiary nitrogen in vBPDP and triazinic nitrogen in vMEL. The dicationic nitrogen of the viologen moiety, which is present in all vCOFs, is represented by the peak at 402.5 eV. Notably, the viologen moiety's redox-active behaviour is underscored by the presence of a substantial peak at 400.5 eV in all samples, which is attributed to the reduced radical cationic nitrogen species ($N^{\bullet+}$) of the viologen unit. For the Cl 2p region, peaks at 197.3 and 198.5 eV were identified, which correspond to Cl $2p_{3/2}$ and Cl $2p_{1/2}$, respectively (Fig. S11†).

2.2 Morphological diversity

To gain a deeper understanding of the morphological differences, we recorded FESEM, HRTEM, and AFM micrographs of these vCOFs (Fig. 2). The FESEM image of vMEL-7 revealed a uniform rod morphology (Fig. 2a and S14†). In contrast, vMEL-8 displayed a well-dispersed spherical-shaped structure (Fig. 2b and S12†) with an average diameter of 5.89 μm, interconnected with the walls of its mesopores (Fig. S13†). On the other hand, the FESEM image of vBPDP-8 showed a rod-shaped morphology (Fig. 2c and S14†), whereas vBPDP-7 exhibited a uniform spherical morphology (Fig. 2d and S12†) with an average diameter of 2.60 μm (Fig. S13†). Hereafter, we labelled rod-shaped (R) vCOFs as vBPDP-8(R) and vMEL-7(R), and spherical-shaped (S) as vBPDP-7(S) and vMEL-8(S). The HRTEM micrographs of all vCOFs exhibited similar observations with FESEM images of vCOFs (Fig. 2e–h). The HRTEM micrographs of vCOFs prominently display clear lattice fringes with spacings of 0.236 nm for vMEL-7(R), 0.235 nm for vMEL-8(S), 0.226 nm for vBPDP-8(R) and 0.223 nm for vBPDP-7(S) (Fig. 2e–h, inset; Fig. S15†), underscoring the highly ordered, layered architecture of vCOFs. Distinct morphology is significantly influenced

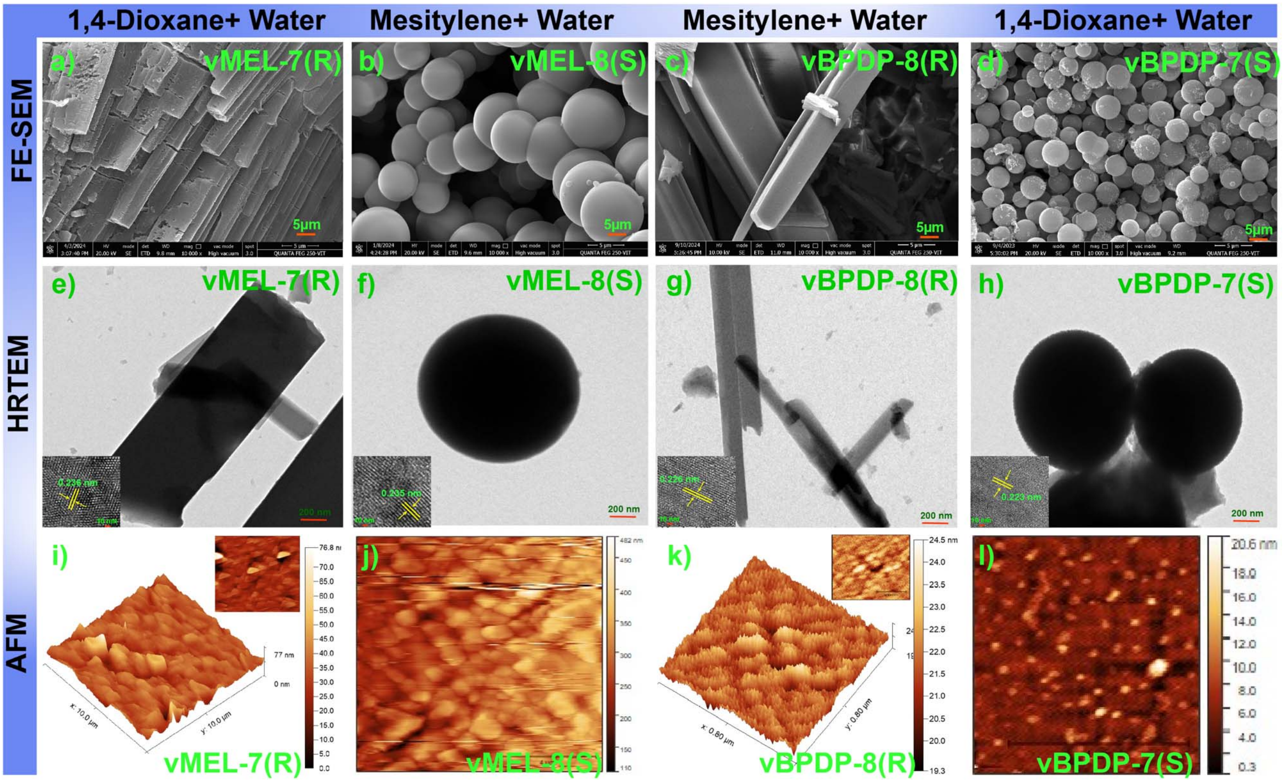

Fig. 2 Microscopic analysis of vCOFs. Field emission scanning electron microscopy (FE-SEM) images of (a) vMEL-7(R), (b) vMEL-8(S), (c) vBPDP-8(R) and (d) vBPDP-7(S). High resolution transmission electron microscope (HRTEM) images of (e) vMEL-7(R), (f) vMEL-8(S), (g) vBPDP-8(R) and (h) vBPDP-7(S). The insets show lattice fringes with interplanar distances. Atomic force microscope (AFM) images of (i) vMEL-7(R); the inset shows a 2D representation of rod morphology, (j) vMEL-8(S), (k) vBPDP-8(R); the inset shows a 2D representation of rod morphology, and (l) vBPDP-7(S).

by the self-assembly process, which is facilitated by kinetic factors and directional interactions that accelerate growth along specific crystallographic axes.[11,20,21]

For instance, the interaction of BPDP with L1 in a polar solvent mixture (1,4-dioxane + water) resulted in the formation of vBPDP-7(S), where the polar environment facilitated charge stabilization and constrained aggregation, thereby encouraging isotropic interactions that led to the creation of spherical micellar structures. In contrast, the interaction between MEL and L1 in a polar solvent was influenced by π–π stacking of the planar cores, promoting anisotropic interactions and rod-like aggregation of vMEL-7(R). It is crucial to recognize that the system might promote the development of spherical aggregates to minimize energy when the interactions between the solvent and the core are highly unfavorable.[16,22] This could account for the uniform spherical shape observed in vMEL-8(S), given that melamine does not dissolve in the less polar solvent mixture of mesitylene and water.

We monitored the time-dependent progression of the morphology of vBPDP-8(R) and vBPDP-7(S) at varying reaction intervals (12 h, 24 h, 36 h, 48 h, and 72 h) (Fig. 3 and S16–S18†). The reaction was halted by removing the reaction containers from the heating oven at each periodic interval, and the samples were subsequently collected for further analysis. The FESEM and HRTEM images demonstrate that the self-assembled rod-shaped morphology of vBPDP-8(R) developed gradually. Structures began to develop in the sample at 12 h and they continued to expand by 24 h. Within 36 h, the crystallites underwent a transition to nanorods and subsequently aggregated into ribbon-like structures. Ultimately, they developed well-defined rod morphologies after 72 h (Fig. 3). In contrast, the FESEM and HRTEM images of vBPDP-7(S) illustrated an alternative growth pathway. During the initial phases of the reaction (12 h and 24 h), the molecules aggregated into small nanofibers (Fig. 3a–g). Progressively, after 48 h, these nanofibers demonstrated a strong propensity for spherical formation, as they expanded and self-assembled in a petal-like fashion as time progressed. At 72 h, a well-defined spherical morphology was observed (Fig. 3h–n). We examined the time-dependent evolution of vBDPDP-8(R) and vBPDP-7(S) at 96 h and 120 h. At 96 h, FESEM images of vBDPDP-8(R) and vBPDP-7(S) revealed well-defined rod-shaped and spherical particles (Fig. S19†), whereas PXRD patterns exhibited broadened peaks and an increasing amorphous background, indicating loss of long-range order. By 120 h, the materials had become predominantly amorphous: PXRD showed only diffuse scattering, and FESEM revealed extensive agglomeration and disappearance of discrete morphologies. Thus, although full crystallinity is achieved by 72 h, heating beyond ≈96 h induces structural collapse and aggregation (Fig. S19†). Uniform mass aggregation was responsible for the construction of the spherical structure in this instance, as the particles were compressed

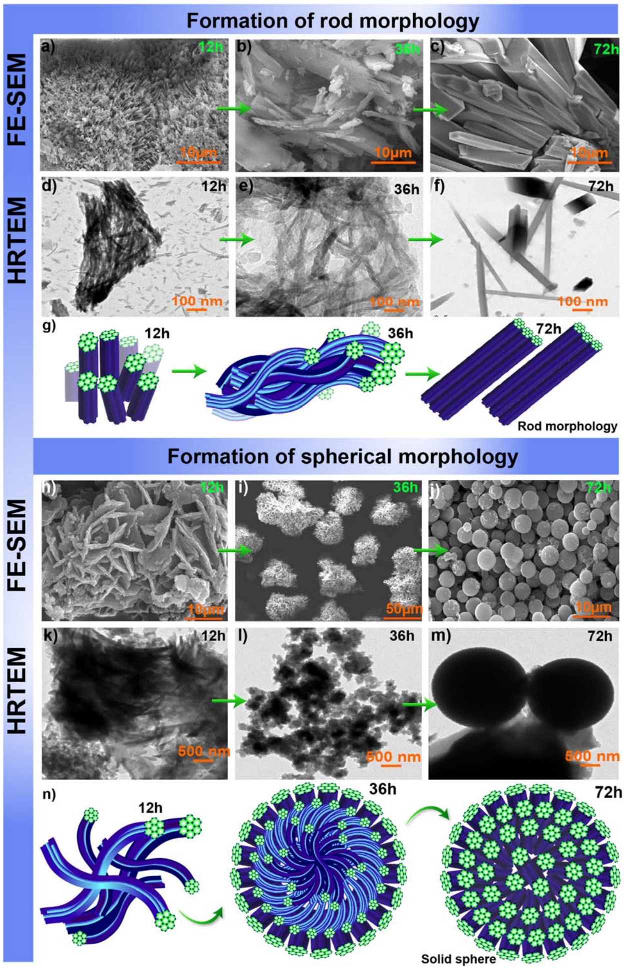

Fig. 3 The mechanism of formation of rod and solid sphere morphologies in vBPDP. (a–c) FESEM and (d–f) HRTEM micrographs of vBPDP-8(R) recorded at different time intervals (12 h, 36 h and 72 h). (g) Schematic reorientation of the formation of rod morphology in vBPDP-8(R). (h–j) FESEM and (k and m) HRTEM micrographs of vBPDP-7(S) recorded at different time intervals (12 h, 36 h and 72 h). (n) Schematic reorientation of the formation of solid spherical morphology in vBPDP-7(S).

into a solid sphere. This process of forming covalent framework materials is exceptional and has been observed rarely. In a nutshell, our study demonstrates that the polarity of the solvent and the structure of the monomer core have a substantial impact on morphology. Specifically, the non-planar BPDP core and the planar MEL core responded differently to polar and nonpolar solvent mixtures.

2.3 Chemical/thermal stability and surface area measurement

We tested the stability of the four vCOFs in boiling water, acidic, and alkaline environments. Each vCOF sample (10 mg) was individually submerged in 10 mL of boiling water (100 °C), 6 M aqueous HCl (25 °C), and 1 M aqueous NaOH (25 °C) solution for 72 h. Subsequently, all the samples were rinsed three times with ethanol and dried properly. The experimental PXRD plots of all treated vCOFs (Fig. S20 and S21†) show that the crystalline peaks are well preserved in the same position with the parent samples, which further verifies the preservation of structural integrity after harsh acid, base and boiling water treatment. These results clearly indicate that all vCOFs exhibit exceptional stability in harsh chemical environments. Thermogravimetric analysis of all vCOFs showed impressive thermal stability, with decomposition temperatures reaching 460 °C, 415 °C, 430 °C and 440 °C for vBPDP-8(R), vBPDP-7(S), vMEL-7(R) and vMEL-8(S), respectively (Fig. S22†). Initial heating showed minor weight losses attributed to the evaporation of trapped solvents. At elevated temperatures, the weight loss increased rapidly, which was consistent with the degradation of the framework. Nitrogen gas adsorption isotherm measurements (77 K) of vCOFs give crucial information regarding the morphological influence on the BET surface area. The surface areas of vBPDP-8(R), vBPDP-7(S), vMEL-7(R), and vMEL-8(S) were 79.89, 35.89, 64.20, and 29.02 $m^2\ g^{-1}$, respectively (Fig. S23†). Rod-shaped vCOFs have a greater BET surface area than spherical-shaped vCOFs, as a result of their higher aspect ratio, which enables a greater amount of exposed surface area. The pore size distributions of the four vCOFs were determined by the BJH method (Fig. S24†). Each material displayed a highly random pore size profile, owing to pore occlusion by their respective counterions. The BJH-derived mean pore diameters for vBPDP-8(R), vBPDP-7(S), vMEL-7(R), and vMEL-8(S) were 2.84 nm, 2.10 nm, 2.59 nm, and 2.25 nm, respectively. These values confirm that the majority of the pores in these materials reside within the mesoporous regime.

2.4 Capture study

To evaluate the adsorption and separation capabilities of these ionic vCOFs in aqueous systems with varying morphologies, a range of ionic and neutral dyes were selected, including anionic dyes: Alizarin Red S (ARS^-), Congo Red (CR^{2-}), and Methyl Orange (MO^-) and neutral dye Fluorescein (FL) (Fig. S25†). The adsorption kinetics of dye contaminants were investigated by introducing 2 mg of each vCOF material to 5 mL aliquots of a 50 ppm aqueous solution of each dye solution at room temperature for a specified duration, followed by filtration to separate the sorbents (details in Section V, ESI†). Subsequently, UV-vis spectroscopy was implemented to evaluate the filtrate concentration. The kinetic plots of rod-shaped vBPDP-8(R) (Fig. 4a) and vMEL-7(R) (Fig. S29†) disclosed that almost 98% and 93% of ARS^- were removed within 30 s (Fig. 4e) and 100% removal happened within 1 min and 2 min, respectively (Fig. S26 and S29†). In stark contrast, the spherical-shaped vBPDP-7(S) and vMEL-8(S) remove 100% of ARS^- dye within 3 min and 5 min, respectively (Fig. 4e and S32, S35†). A similar kind of trend was observed in the kinetic study and removal efficiencies for two other anionic dyes, CR^{2-} and MO^- (Fig. 4f and g). vBPDP-8(R) exhibited 100% removal of CR^{2-} and MO^- within 2 min and 40 s, respectively (Fig. S27 and S28†), whereas vMEL-7(R) achieved 100% removal of CR^{2-} and MO^- within 3 min and 2 min, respectively (Fig. S30 and S31†). In contrast, spherical-shaped vBPDP-7(S) and vMEL-8(S) exhibited complete removal of CR^{2-} and MO^- (Fig. S32 and S37†) in

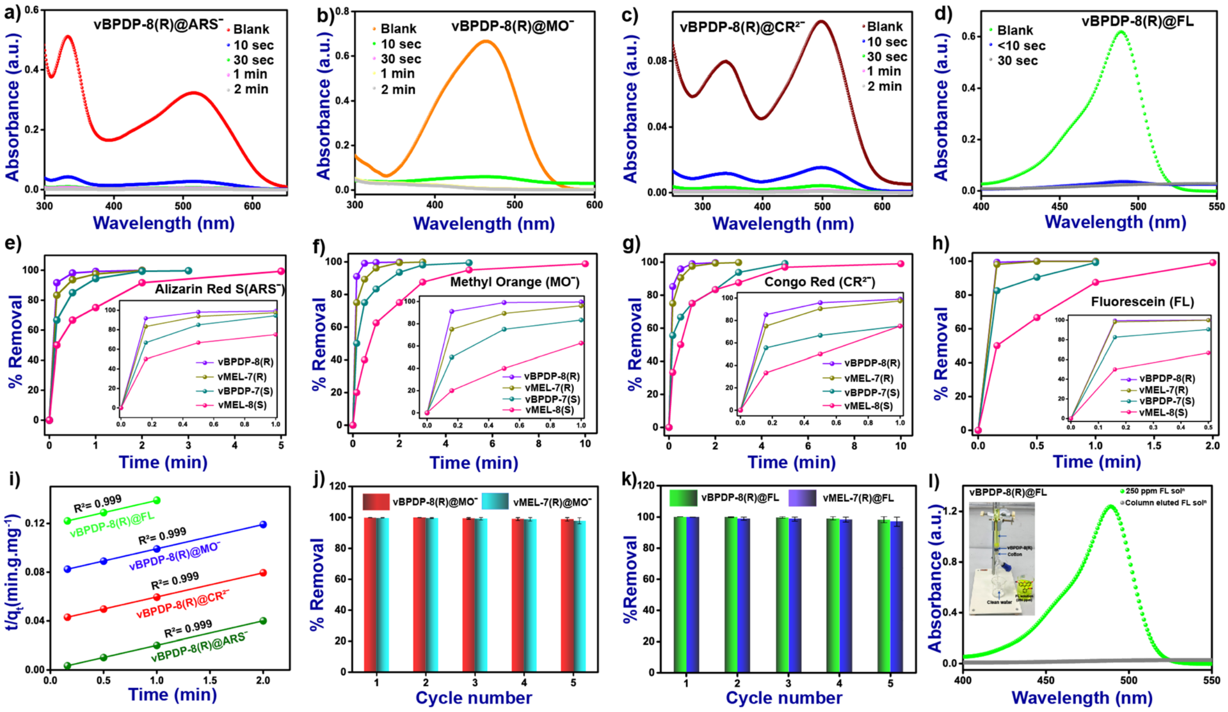

Fig. 4 UV-visible spectra in the presence of vBPDP-8(R) at different time interval for the aqueous solution of (a) Alizarin Red S (ARS), (b) Methyl Orange (MO), (c) Congo Red (CR) and (d) Fluorescein (FL). (e–h) The comparison between all four vCOFs depending on their removal efficiencies in % of toxic dyes from the water at different time intervals. (i) Pseudo second order linear fit plots of vBPDP-8(R) for all dyes. (j) Recyclability experimental results of vBPDP-8(R) and vMEL-7(R) for MO dye removal. (k) Recyclability experimental results of vBPDP-8(R) and vMEL-7(R) for FL dye removal. (l) Image and UV-vis spectra of the 500 ppm FL solution before and after passing through the vBPDP-8(R) loaded packed column.

a much longer time (10 min). The aforementioned discussion has led to the conclusion that all vCOFs exhibited ultrafast adsorption of anionic toxic dyes and can be considered competitive with cutting-edge scavengers. The adsorption processes of these anionic dyes can fit well with the pseudo-second-order kinetic models, as evidenced by the strong linear relationship between t/Q_t *vs.* t, tabulated in the ESI (Table S2†). The maximum adsorption capacities ($Q_{\max}$) of vBPDP-8(R) were 362.35, 457.76 and 1161.78 mg g^{-1} for ARS$^-$, CR^{2-}, and MO$^-$ respectively. Similarly, the maximum adsorption capacities of vMEL-7(R) were 338.46, 417.05 and 989.94 mg g^{-1} for ARS$^-$, CR^{2-} and MO$^-$, respectively (Table S2, ESI†). The adsorption of ARS$^-$, CR^{2-}, and MO$^-$ by vBPDP-8(R) was found to align with the Langmuir isotherm model, indicating complete monolayer coverage and had a strong correlation with the experimental observations and capture studies (Fig. S44 and Table S3†). It should highlight that the adsorption capacity of vBPDP-8(R) and vMEL-7(R) for MO$^-$ is unprecedented and exceptionally superior to that of commercially available materials such as activated carbon[23] and porous materials, including polypyrrole–chitosan composites,[24] 3D-printed COF-GO foams,[25,26] MOF aerogels,[27] zeolites,[28,29] α-Al$_2$O$_3$, and Fe$_3$O$_4$ nanoparticles[30,31] (Table S9, ESI†). It is noteworthy to mention that vBPDP-8(R) exhibited the highest removal efficiency and capture capacity for anionic dyes among all vCOFs, followed by vMEL-7(R) > vBPDP-8(S) > vMEL-7(S). Moreover, vBPDP-8(R) can be considered as one of the efficient or best scavenging porous materials (COFs, MOFs, POPs *etc.*) for anionic dyes due to its excellent removal efficiency and capture capacity (Table S10, ESI†). To assess the selectivity for anionic dyes, vBPDP-8(R) (2 mg) was exposed to aliquots of a 50 ppm aqueous solution of the cationic dyes methylene blue (MLB$^+$) and rhodamine B (RhB$^+$). Kinetic studies revealed that vBPDP-8(R) was less effective in removing cationic dyes from water (Fig. S38 and S39†). These findings strongly suggest that the vCOFs are selective for the removal of anionic dyes. The rigorous evaluation of our findings has demonstrated that rod-shaped structures are more effective at removing anionic dyes than spherical-shaped vCOFs. Possibly, the greater surface area of rod-shaped structures with many sites for π–π conjugation attracts dye molecules, leading to better adsorption efficiency.

We also conducted adsorption experiments on the hydrophilic neutral dye fluorescein (FL). Prior to the adsorption experiment, the hydrophilicity of all four vCOFs was confirmed by contact angle measurements in 3 M NaOH solution, which showed a significant decrease in angles within 5 s (ESI, Video S1†), indicating the highly hydrophilic nature of vCOFs. To our surprise, we found that vBPDP-8(R) removed approximately 99% of FL in less than 10 s, one of the fastest adsorption rates. vMEL-7(R), vMEL-8(S) and vBPDP-7(S) each removed FL completely within 60 s (Fig. 4h). The adsorption kinetics (Fig. S40–S43†) aligned well with pseudo-second-order models, as indicated by the linear t/Q_t *versus* t relationship. vBPDP-8(R) and vMEL-7(R) achieved impressive FL dye capture capacities of

1237.40 mg g^{-1} and 1024.08 mg g^{-1} respectively. As per our knowledge, their capture efficiencies are highest among all porous and coordination polymers, including MOFs, COFs, and POPs (Tables S7 and S8, ESI†). Spherical-shaped vBPDP-7(S) and vMEL-8(S) captured FL dye with adsorption capacities of 863.89 and 795.51 mg g^{-1}, respectively (Table S2, ESI†). This indicates that rod-shaped morphologies are more favourable to FL capture than spherical ones. 3D confocal microscopy images demonstrated dye adsorption in the vCOFs' peripheral and surface regions (Fig. S46†). Furthermore, XPS analyses were performed on vBPDP-8(R) and vMEL-7(R) following ARS^- adsorption. In the survey spectra of vBPDP-8(R)@ARS^- and vMEL-7(R)@ARS^-, the original Cl 2p signals were absent and replaced by a new S 2p feature, providing direct evidence for the exchange of chloride ions with alizarin sulfonate anions. Peak deconvolution of the S 2p region revealed components at approximately 167.8 eV and 169.2 eV, consistent with sulfonate functionalities (Fig. S47, ESI†). These spectroscopic data furnish definitive chemical validation of the COFs and substantiate the specific COF/dye interactions.

From the aforementioned investigation, it is evident that vCOFs can achieve dye adsorption through a selective charge separation mechanism. To confirm this, the adsorption characteristics of vBPDP-8(R) were assessed in a mixed solution of MO^-/MLB^+. Surprisingly, in 2 min, the entire MO^- was adsorbed, with a removal rate of 98.7%, as shown in Fig. S45.† In contrast, a small amount of MLB^+ was adsorbed, with a removal rate of 22.7%. The preferential and selective adsorption of MO^- was validated by the concurrent change in solution color from dark green to blue (Video S3, ESI†). Thus, it is evident that vBPDP-8(R) is one of the most effective adsorbents for the selective capture of hazardous dyes among the four vCOFs. Therefore, to conduct a more comprehensive scrutiny, we selected ARS^- (an anionic dye) and FL (a neutral dye) as model dyes. To demonstrate the practical applicability of vCOFs, we explored the effects of pH and the reusability of the adsorbent. The removal efficiency for ARS^- and FL remained above 99% at a wide range of pH levels (Fig. S48†). It was noted that the efficiencies of dye removal were minimally influenced by the pH of the samples, suggesting that the performance of vCOFs was not influenced by the matrices of the samples. Reusability is a critical factor in evaluating the practical potential of adsorption media. To conduct a more comprehensive analysis, we selected vBPDP-8(R) as the model compound and ARS^- (an anionic dye) and FL (a neutral dye) as model dyes. The removal efficiency of both ARS^- and FL demonstrated virtually no decrease after five consecutive adsorption–removal–regeneration cycles (Fig. 4j and k), highlighting the exceptional recyclability of vCOFs. After dye adsorption and removal, the PXRD peak positions were unchanged (Fig. S49a†) in comparison to the pristine vBPDP-8(R). The BET surface area of vBPDP-8(R) remained significantly unchanged after five successive adsorption–desorption cycles, measuring 74.76 m^2 g^{-1} compared to the pristine value of 79.89 m^2 g^{-1}. However, after seven cycles, the surface area decreased to 44.12 m^2 g^{-1} (Fig. S50†). These results highlight the exceptional stability and effective reusability of vBPDP-8(R) over five complete cycles. Furthermore, the surface morphology remained the same after multiple adsorption–removal–regeneration cycles (Fig. S49b†), indicating the exceptional stability and long-term potential of vBPDP-8(R) for real-time wastewater treatment applications.

Moreover, a chromatographic column was constructed with vBPDP-8(R) and utilized for the removal of toxic organic dyes from water (Fig. 4l). A 250 ppm stock solution of each dye (ARS^- and FL) was passed through the column (Video S2, ESI†). The results indicated that the absence of ARS^- and FL peaks in the collected colorless water demonstrates the effective removal of toxic dyes using vBPDP-8(R) (Fig. S51 and S52†). To assess the recyclability of vBPDP-8(R), the column was regenerated by washing it with a 3 M HCl solution, followed by distilled water/acetone and utilized for the second cycle of dye removal. Upon assessment of these findings, vBPDP-8(R) has considerable potential as a water remediation agent owing to its elevated adsorption capabilities for toxic anionic and neutral organic dyes.

2.5 DFT studies

The DFT simulation was performed with a focus on a single polymeric network. The interactions at the molecular scale between vBPDP and vMEL and the dyes (anionic – ARS^-, cationic – MB^+ and neutral – FL were chosen for the DFT studies) were examined with Gaussian 16.0 software (details in the ESI†).[32] We determined the highest occupied molecular orbital (HOMO) and lowest unoccupied molecular orbital (LUMO) for the geometrically optimized single polymeric networks of vBPDP and vMEL (Fig. 5a and b). The donor–acceptor architecture of vBPDP allows charge transfer because the HOMO is on the viologen unit (L1) and the LUMO on the BPDP unit (Fig. 5c). The yellow-red contrast on the Molecular Electrostatic Potential (MESP) map confirms the role of viologen units as the donor, highlighting its active participation in interactions. After optimization, vBPDP assumes a propeller-like configuration, a geometry that enhances adsorption efficiency due to its unique structural advantages. Fig. 5b indicates that vMEL, optimized at the same theoretical level, has a planar structure with uniform HOMO and LUMO distribution throughout the unit. The analysis of binding affinity demonstrates that vBPDP has robust interactions with FL and ARS^- dyes, with binding energies of −55.33 eV and −45.42 eV, respectively, indicating a higher affinity for FL. The interaction with methylene blue (MB^+) is the weakest, with a value of 4.2 eV (Fig. 5e–g). Natural Bond Orbital (NBO) analysis reveals that ARS^-/vBPDP interactions are non-covalent, involving the oxygen atoms of ARS^- and the C–C and C–H bonds of vBPDP (Table S4, ESI†). For FL, interactions occur between the oxygen lone pairs of FL and the N–H and C–H bonds of vBPDP (Table S5, ESI†). The results of the Non-Covalent Interaction (NCI) analysis and reduced density gradient (RDG) plots are further substantiated by the presence of green and blue peaks, which suggest strong, reversible van der Waals interactions with FL and ARS^- (Fig. 5h and j). Conversely, the red peaks in the RDG plot for MB^+ suggest weak or repulsive interactions (Fig. 5i). Similarly, vMEL exhibits robust interactions with ARS^- and FL,

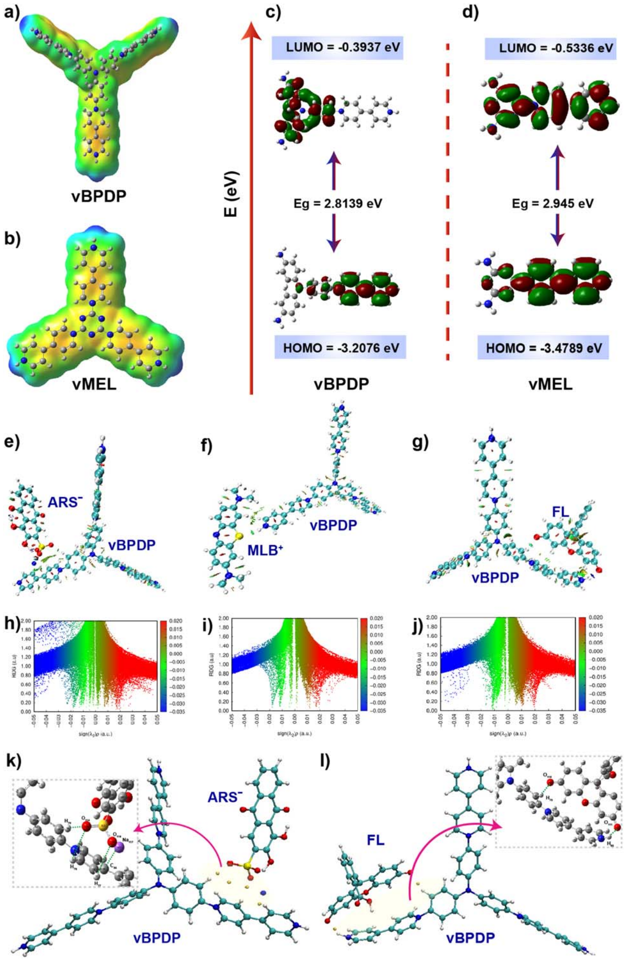

Fig. 5 Electrostatic potential (ESP) diagram of an optimized fragment of (a) vBPDP and (b) vMEL. HOMO–LUMO energy profile of (c) vBPDP and (d) vMEL. Molecular-level interaction of vBPDP with (e) alizarin red S (anionic dye), (f) methylene blue (cationic dye) and (g) fluorescein (neutral dye). Reduced density gradient plots of vBPDP interacting with (h) alizarin red S (anionic dye), (i) methylene blue (cationic dye) and (j) fluorescein (neutral dye). QTAIM-mapped bond critical points between (k) vBPDP and ARS^- and (l) vBPDP and FL.

with binding energies of −40.86 eV and −28.83 eV, respectively. However, its interaction with MB^+ is very weak, with a binding energy of 2.48 eV. NBO analysis for vMEL with ARS^- reveals that reversible interactions occur between the oxygen atoms of ARS^- and the C–C bonds of vMEL (Table S5, ESI†). For FL, interactions involve the oxygen lone pairs of the dye and the C–H bonds in vMEL (Table S7, ESI†). RDG plots display green and blue peaks for ARS^- and FL, indicating strong van der Waals interactions, while red peaks for MB^+ indicate repulsion (Fig. S53–S55†). Thus, findings on binding energy and NBO analyses indicate that neutral and anionic dyes exhibit more robust interactions with vCOFs. Donor–acceptor properties of vBPDP frameworks exhibit greater affinity towards these dyes than the vMEL framework, which facilitates more charge transport. The above simulation data strongly support our experimental findings and reinforce our comprehension of the selective and efficient capture performance of vCOFs with anionic and neutral dyes. Furthermore, the Quantum Theory of Atoms in Molecules (QTAIM) was employed to conduct a detailed atomic-level analysis of the interactions between vCOFs and dye molecules, providing insights into the nature of intermolecular contacts (details in ESI, Section SVI†). vBPDP@ARS^- exhibits four bond critical points (BCPs) *versus* two for vBPDP@FL, reflecting a more intricate interaction network (Fig. 5k and l). In the case of ARS^- and FL, the electron density $\rho(r)$ indicates multiple moderate hydrogen bonds rather than isolated strong contacts (Table S8†). Furthermore, the summed total energy densities $H(r)$ for vBPDP@ARS^- and vBPDP@FL (Table S8, ESI†), indicate that vBPDP binds ARS^- with an extensive and uniform network of moderately strong interactions, resulting in slightly superior overall binding compared to FL. Similarly, for vMEL, QTAIM descriptors indicate that both ARS^- and FL form three BCPs with vMEL frameworks (Fig. S56, S57 and Video S5†). Specifically, all key topological parameters confirm that the vMEL@ARS^- complex exhibits a more uniformly distributed and energetically favorable interaction compared to vMEL@FL (Table S8, ESI†). In summary, the QTAIM analysis suggests that both vBPDP and vMEL frameworks establish a more extensive and uniform network of moderately strong interactions with ARS^-, which leads to marginally stronger overall binding than with FL.

3. Conclusion

In conclusion, we have successfully synthesized and developed two crystalline, chemically stable viologen-based covalent organic frameworks (vBPDP and vMEL) with unique morphologies. The monomer core type (planar or nonplanar) and solvent polarity have a strong influence on the morphology, which was driven by π–π stacking and anisotropic interactions. Triazine-based vMEL COFs exhibited a rod-shaped morphology in 1,4-dioxane/water and spherical structures in mesitylene/water, whereas triphenylamine-based vBPDP COFs exhibited the opposite trend in these solvent systems. This investigation offers a thorough examination of the time-dependent self-assembly mechanisms that are responsible for the formation of these morphologies, and the influence of the monomer core structure, as well as the solvent type, on the formation of vCOFs. Furthermore, the comparative morphology-based investigation of these frameworks was facilitated to detoxify toxic organic dyes (both anionic and neutral) from contaminated water. Rod-shaped vCOFs [vBPDP-8(R) and vMEL-7(R)] achieved very high adsorption of anionic methyl orange (1161.78 and 989.94 mg g^{-1}) and neutral fluorescein dye (1237.40 and 1024.08 mg g^{-1}). Conversely, the adsorption rates of spherical-shaped vCOFs were sluggish. These results were also confirmed by the DFT investigation, which suggested that the dye molecules have robust non-covalent interactions with the framework. Additionally, the Quantum Theory of Atoms in Molecules (QTAIM) was implemented to perform a comprehensive atomic-level examination of the interactions between vCOFs and dye molecules, thereby offering a detailed understanding of the nature of intermolecular contacts. These vCOFs exhibited high recyclability for the removal of both anionic dyes across multiple adsorption cycles. We anticipate that this adsorption process can be easily scaled up for real-world applications, and the cationic porous polymer reported here will significantly contribute to the development of suitable adsorptive media for sustainable wastewater treatment in the future.

4. Experimental

The Experimental section is discussed in the ESI.†

Data availability

All relevant data supporting this article have been included within the article and its ESI† files. Additional raw data can be provided by the corresponding author upon reasonable request.

Conflicts of interest

There are no conflicts to declare.

Acknowledgements

PJ, AW and MV acknowledge VIT, Vellore, for the Teaching and Research Assistant (TRA) fellowship. TP acknowledges the financial assistance from CSIR, research grant 01/3130/23/EMR-II from the Government of India. We acknowledge VIT CIF for the FE-SEM, HRTEM, and AFM instruments. We also acknowledge the CCE instrumentation facilities.

Notes and references

1 P. J. J. Alvarez, C. K. Chan, M. Elimelech, N. J. Halas and D. Villagrán, *Nat. Nanotechnol.*, 2018, **13**, 634–641.
2 R. P. Schwarzenbach, B. I. Escher, K. Fenner, T. B. Hofstetter, C. A. Johnson, U. von Gunten and B. Wehrli, *Science*, 2006, **313**, 1072–1077.
3 Y. Song, J. Phipps, C. Zhu and S. Ma, *Angew. Chem., Int. Ed.*, 2023, **62**, e202216724.
4 A. K. Mohammed and D. Shetty, *Environ. Sci.:Water Res. Technol.*, 2021, **7**, 1895–1927.
5 M. K. Tufail, M. Ifrahim, M. Rashid, I. Ul Haq, R. Asghar, U. T. Uthappa, M. Selvaraj and M. Kurkuri, *Sep. Purif. Technol.*, 2025, **354**, 128739.
6 M. Liu, Q. Xu and G. Zeng, *Angew. Chem., Int. Ed.*, 2024, **63**, e202404886.
7 P. Jhariat and T. Panda, *Mater. Adv.*, 2024, **5**, 4055–4077.
8 J. Sakamoto, J. van Heijst, O. Lukin and A. D. Schlüter, *Angew. Chem., Int. Ed.*, 2009, **48**, 1030–1069.
9 M. S. Lohse and T. Bein, *Adv. Funct. Mater.*, 2018, **28**, 1705553.
10 S. Karak, K. Dey and R. Banerjee, *Adv. Mater.*, 2022, **34**, 2202751.
11 K. T. Tan, S. Ghosh, Z. Wang, F. Wen, D. Rodríguez-San-Miguel, J. Feng, N. Huang, W. Wang, F. Zamora, X. Feng, A. Thomas and D. Jiang, *Nat. Rev. Methods Primers*, 2023, **3**, 1.
12 S. Kandambeth, V. Venkatesh, D. B. Shinde, S. Kumari, A. Halder, S. Verma and R. Banerjee, *Nat. Commun.*, 2015, **6**, 6786.
13 A. K. Mohammed, S. Usgaonkar, F. Kanheerampockil, S. Karak, A. Halder, M. Tharkar, M. Addicoat, T. G. Ajithkumar and R. Banerjee, *J. Am. Chem. Soc.*, 2020, **142**, 8252–8261.
14 B. J. Smith, L. R. Parent, A. C. Overholts, P. A. Beaucage, R. P. Bisbey, A. D. Chavez, N. Hwang, C. Park, A. M. Evans, N. C. Gianneschi and W. R. Dichtel, *ACS Cent. Sci.*, 2017, **3**, 58–65.
15 H. S. Sasmal, A. Kumar Mahato, P. Majumder and R. Banerjee, *J. Am. Chem. Soc.*, 2022, **144**, 11482–11498.
16 B. Gole, V. Stepanenko, S. Rager, M. Grüne, D. D. Medina, T. Bein, F. Würthner and F. Beuerle, *Angew. Chem., Int. Ed.*, 2018, **57**, 846–850.
17 P. Jhariat, A. K. U, A. Warrier, A. P. Sunda, S. Das, S. Sarfudeen, V. M. Dhavale and T. Panda, *ACS Appl. Mater. Interfaces*, 2024, **16**, 23387–23395.
18 Y. J. Lee, S. N. Talapaneni and A. Coskun, *ACS Appl. Mater. Interfaces*, 2017, **9**, 30679–30685.
19 P. Jhariat, A. Warrier, A. Sasmal, S. Das, S. Sarfudeen, P. Kumari, A. K. Nayak and T. Panda, *Nanoscale*, 2024, **16**, 5665–5673.
20 A. Halder, S. Kandambeth, B. P. Biswal, G. Kaur, N. C. Roy, M. Addicoat, J. K. Salunke, S. Banerjee, K. Vanka, T. Heine, S. Verma and R. Banerjee, *Angew. Chem., Int. Ed.*, 2016, **55**, 7806–7810.
21 A. F. M. El-Mahdy, C. Young, J. Kim, J. You, Y. Yamauchi and S.-W. Kuo, *ACS Appl. Mater. Interfaces*, 2019, **11**, 9343–9354.
22 J.-G. Jia, C.-C. Zhao, Y.-F. Wei, Z.-M. Zhai, S.-S. Bao, A. J. Jacobson, J. Ma and L.-M. Zheng, *J. Am. Chem. Soc.*, 2023, **145**, 23948–23962.
23 N. U. M. Nizam, M. M. Hanafiah, E. Mahmoudi, A. A. Halim and A. W. Mohammad, *Sci. Rep.*, 2021, **11**, 8623.
24 T.-H. Dao, T.-Q.-M. Vu, N.-T. Nguyen, T.-T. Pham, T.-L. Nguyen, S.-i. Yusa and T.-D. Pham, *Langmuir*, 2020, **36**, 13001–13011.
25 C. Li, P. Guggenberger, S. W. Han, W.-L. Ding and F. Kleitz, *Angew. Chem., Int. Ed.*, 2022, **61**, e202206564.
26 T. Selkälä, T. Suopajärvi, J. A. Sirviö, T. Luukkonen, P. Kinnunen, A. L. C. B. de Carvalho and H. Liimatainen, *ACS Appl. Mater. Interfaces*, 2020, **12**, 27745–27757.
27 H. Ukani, S. Mehra, B. Parmar, A. Kumar, I. Khan, O. A. El Seoud and N. Malek, *Ind. Eng. Chem. Res.*, 2023, **62**, 5002–5014.
28 E. Pérez-Botella, S. Valencia and F. Rey, *Chem. Rev.*, 2022, **122**, 17647–17695.
29 A. Hamd, M. Shaban, G. M. Al-Senani, M. N. Alshabanat, A. Al-Ghamdi, A. R. Dryaz, S. A. Ahmed, R. El-Sayed and N. K. Soliman, *Sci. Rep.*, 2023, **13**, 8082.
30 B. Saha, S. Das, J. Saikia and G. Das, *J. Phys. Chem. C*, 2011, **115**, 8024–8033.
31 P. Kaur and M. S. Bakshi, *ACS Appl. Polym. Mater.*, 2024, **6**, 8659–8670.
32 M. Varghese, J. M. Thomas, A. Y. Alzahrani and R. Thomas, *Z. Phys. Chem.*, 2024, **238**, 1731–1751.